Tangential Velocity Estimation Using Separated Non-Coherent Automotive Radar Array

M. Shifrin, J. Tabrikian, and I. Bilik
School of Electrical and Computer Engineering
Ben-Gurion University of the Negev, Beer-Sheva 84105, Israel

***Abstract*—Automotive radar is the main sensor enabling autonomous driving and active safety features. It is required to provide high-resolution information on the vehicle's surroundings, accurately localize obstacles, and estimate their velocity in two dimensions. Conventional automotive radars operating in the far-field regime estimate only the target's radial velocity and cannot obtain its tangential velocity. However, the near-field propagation conditions allow the tangential radar target velocity estimation. This work leverages our previous identifiability study, where the conditions for the tangential velocity estimation have been stated, and proposes an iterative algorithm for tangential velocity estimation in automotive near-field scenarios using a non-coherent separated sensor array. The performance of the proposed approach is evaluated, and its efficiency and near-field synthetic aperture (NFSA) dependency is demonstrated via simulations.**

***Index Terms*—Tangential velocity estimation, near-field, automotive radar, Cramér-Rao bound, separated array, non-coherent arrays**

I. Introduction

Automotive radars enable reliable sensing capabilities in harsh weather and poor lighting conditions, providing essential environmental perception for autonomous vehicles [1–3]. As a result, automotive radar has emerged as a crucial component of modern advanced driver assistance systems (ADAS) and autonomous driving technologies [4–8]. Conventionally, radars estimate the direction-of-arrival (DOA), range, and radial velocity of targets [9]. However, accurate estimation of two-dimensional (2D) target velocities has become increasingly important in automotive applications [10, 11]. In particular, precise 2D velocity estimation is critical in complex driving environments such as intersections, merging lanes, and dense urban traffic, where comprehensive velocity information significantly enhances safety and navigation accuracy [12].

Conventional automotive radars cannot directly estimate the tangential component of a target's 2D velocity [13]. Several approaches addressing 2D velocity estimation have been introduced in the literature, primarily in airborne radar applications [14–17]. In automotive applications, radar-camera sensor fusion has been proposed to estimate target lateral velocities [18]. Moreover, automotive radar-based 2D velocity estimation techniques leveraging prior knowledge from distributed point cloud detections of moving targets have been explored in [19, 20]. In addition, target tracking can be used for 2D velocity estimation [21, 22]. However, target tracking requires a long observation time, which is limited by the ADAS requirement for real-time decision-making. Moreover, during long observation time, the assumption of the target's linear and constant velocity may be invalid, which degrades the target's parameters estimation performance. Alternative works have investigated the use of multiple radar arrays to achieve accurate 2D velocity information [23–26].

Estimating the target tangential velocity is feasible for automotive radar systems operating in the near-field regime. Various approaches have explored the near-field propagation conditions in the synthetic aperture radar (SAR) framework [27–30] and analysis of Cramér-Rao bound (CRB) on the estimation of static targets coordinates [31–37]. Our previous work [38], derived the CRB for tangential velocity estimation using a uniform linear arrays (ULA) under the near-field model, emphasizing its dependence on the target range and DOA. However, the ULA aperture is small due to practical constraints, hence it becomes difficult to obtain the target angular motion throughout the observation time. Therefore, the ULA model mostly includes sign ambiguous tangential velocity estimation information. Therefore, this work addresses this ambiguity by considering the non-coherent wide aperture separated array for automotive radar.

This work extends our previous work [38] and proposes an iterative algorithm for tangential velocity estimation based on the maximum likelihood (ML) estimator using a wide aperture separated array model. The performance of the proposed algorithm is evaluated via simulations, and it is shown that the algorithm is asymptotically efficient.

II. Automotive Separated Radar Array Model

This section presents an automotive radar data model for the wide aperture separated array configuration, consisting of two non-coherent subarrays. Consider a single-input multiple-output (SIMO) automotive radar on the host vehicle, observing a single target with relative radial and tangential velocity components at time $t = 0$, v_r, v_θ, respectively. In general, radar clutter can be modeled as multiple targets [39]. This work introduces a fundamentally new approach, and therefore, a single target scenario is considered for the clarity of the presentation. The radar platform consists of a transmitter located at the origin and a separated array of sensors, comprising two subarrays separated by a distance $\bar{D}$, as depicted in Fig. 1. The elements within each subarray are spaced at $\lambda/2$, where λ is the radar wavelength. The l^{th} sensor location in the q^{th} subarray is

$$d_{q,l} = \bar{D}\left(q - \frac{1}{2}\right) + \frac{\lambda}{2}\left(l - \frac{L-1}{2}\right) . \quad (1)$$

The second-order Taylor expansion of the target range from the l^{th} sensor in the q^{th} subarray is

$$r_{q,l}(t) \approx r + v_r t - d_{q,l}\sin\theta + \frac{1}{2r}\left(v_\theta t - d_{q,l}\cos\theta\right)^2 \ , \quad (2)$$

and the transmitter-to-target-to-receiver delay of the radar array is

$$\tau_{q,l}(t) \approx \frac{2r}{c} + \frac{2v_r t}{c} - \frac{d_{q,l}\sin\theta}{c} + \frac{v_\theta^2 t^2}{2rc} + \frac{1}{2rc}\left(v_\theta t - d_{q,l}\cos\theta\right)^2 \ , \quad (3)$$

where c is the electromagnetic wave propagation speed.

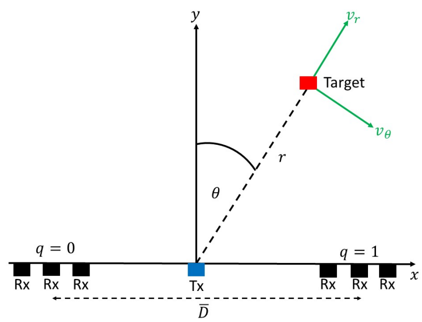

Fig. 1: Schematic representation of the wide aperture separated radar array in a single-target scenario.

The radar transmits a sequence of K linear frequency modulated (LFM) chirps of duration, T_{c}, with pulse repitition interval (PRI), $T_{\text{PRI}} > T_{\text{c}}$. The signal at the k^{th} transmitted chirp, at time $t \in \left[T_k - \frac{T_{\text{c}}}{2}, T_k + \frac{T_{\text{c}}}{2}\right]$, is given by:

$$s_k(t) = e^{j\pi a (t-T_k)^2} e^{j\omega_c t} \ , \ \ \forall k = 0, \ldots, K-1 \ , \quad (4)$$

where $T_k = \left(k - \frac{K-1}{2}\right) T_{\text{PRI}}$. The chirp slope, a, satisfies $aT_{\text{c}} = B$, and B is the signal bandwidth. The signal's carrier angular frequency is $\omega_c = 2\pi f_c$, where f_c is the radar carrier frequency, satisfying $\lambda f_c = c$.

The received k^{th} chirp of the signal at time t, and the l^{th} sensor of the q^{th} subarray is given by

$$\tilde{x}_{q,l,k}(t) = \bar{\alpha}_q e^{j\pi a (t-T_k-\tau_l(t))^2} e^{j\omega_c (t-\tau_l(t))} + \tilde{w}_{l,k}(t) \ , \quad (5)$$

where the complex amplitudes, $\{\bar{\alpha}_q\}$, include the propagation path loss and the target reflection coefficient. The complex amplitudes are assumed to be different for each subarray in order to avoid the coherency requirement, which is often difficult to satisfy in practice. The sequence $\{\tilde{w}_{q,l,k}(t)\}$ is a circularly symmetric complex white Gaussian noise along q, k, l, and t. The k^{th} received chirp at the l^{th} sensor of the q^{th} subarray, is simplified by multiplication of (5) with (4) as

$$x_{q,l,k}(t) = \tilde{x}_{q,l,k}(t) s_k^*(t) = \bar{\alpha}_q e^{-j(2\pi a (t-T_k)+\omega_c)\tau_l(t)} e^{j\pi a \tau_l^2(t)} + w_{q,l,k}(t) \ , \quad (6)$$

where $w_{q,l,k}(t) = \tilde{w}_{q,l,k}(t) s_k^*(t)$. By substitution of (3) into (6), and assuming, $e^{j\pi a \tau_l^2(t)} \approx e^{j4\pi a \frac{r^2}{c^2}}$, the data model can be rewritten as

$$x_{q,l,k}(t) = \tilde{\alpha}_q e^{-j2\pi a (t-T_k)\left(\frac{2r}{c} + \frac{2v_r}{c}t - \frac{\sin\theta}{c} d_{q,l}\right)} \times e^{-j\omega_c\left(\frac{2v_r}{c}t - \frac{d_{q,l}\sin\theta}{c} + \frac{v_\theta^2}{rc}t^2 - \frac{v_\theta\cos\theta}{rc} d_{q,l} t + \frac{\cos^2\theta}{rc} d_{q,l}^2\right)} + w_{q,l,k}(t) \ , \quad (7)$$

where $\tilde{\alpha}_q = \bar{\alpha}_q e^{j4\pi a \frac{r^2}{c^2}} e^{-j\omega_c \frac{2r}{c}}$. The radar echo in (7) is sampled at the time instances, $t = T_k + t_n$, and (7) can be rewritten as

$$X_{q,l,n,k} = \tilde{\alpha}_q e^{-j2\pi a \frac{2r}{c} t_n} e^{-j2\pi a \frac{2v_r}{c} T_k t_n} e^{j2\pi a \frac{\sin\theta}{c} d_{q,l} t_n} \times e^{-j\omega_c \frac{2v_r}{c} T_k} e^{j\frac{2\pi\sin\theta}{\lambda} d_{q,l}} e^{-j\frac{\omega_c v_\theta^2}{rc} T_k^2} \times e^{j\frac{2\pi v_\theta\cos\theta}{r\lambda} d_{q,l} T_k} e^{-j\frac{2\pi\cos^2\theta}{r\lambda} d_{q,l}^2} + W_{q,l,n,k} \ . \quad (8)$$

Substituting (1) into (8) results in

$$X_{q,l,n,k} = \alpha_q e^{-j2\pi a \frac{2r}{c} t_n} e^{-j2\pi a \frac{2v_r}{c} T_k t_n} e^{j2\pi a \frac{\bar{D}_q \sin\theta}{c} t_n} \times e^{-j\omega_c \frac{2v_r}{c} T_k} e^{j\frac{2\pi\sin\theta}{\lambda} d_l} e^{-j\frac{\omega_c v_\theta^2}{rc} T_k^2} \times e^{j\frac{2\pi \bar{D}_q \cos\theta v_\theta}{r\lambda} T_k} e^{j\frac{2\pi v_\theta\cos\theta}{r\lambda} d_l T_k} \times e^{-j\frac{4\pi \bar{D}_q \cos^2\theta}{r\lambda} d_l} + W_{q,l,n,k} \ , \quad (9)$$

where $\alpha_q = \tilde{\alpha}_q e^{-j\frac{\pi \bar{D}_q^2 \cos^2\theta}{2r\lambda}} e^{j\frac{2\pi \bar{D}_q \sin\theta}{\lambda}}$, $d_l = \frac{\lambda}{2}\left(l - \frac{L-1}{2}\right)$, and $\bar{D}_q = \bar{D}(q - 1/2)$.

The resulting radar data model in (9) can be rewritten as two vectors, $\mathbf{x}_0$ and $\mathbf{x}_1$, corresponding to each subarray, where $\mathbf{x}_q \in \mathbb{C}^{LNK}$, and

$$\mathbf{x}_q = \alpha_q \boldsymbol{\eta}(r, v_r, \theta) \odot \mathbf{b}_q(r, v_r, v_\theta, \theta) \odot \mathbf{z}_q(r, v_\theta, \theta) + \mathbf{w}_q \ , \quad (10)$$

where $\mathbf{w}_0$ and $\mathbf{w}_1$ are i.i.d., $CN\left(\mathbf{0}, \sigma_w^2 \mathbf{I}_{LNK}\right)$ distributed. The conventional data vector, $\boldsymbol{\eta}(r, v_r, \theta)$, satisfies

$$\boldsymbol{\eta}(r, v_r, \theta) = \boldsymbol{\eta}_{\text{R}}(\theta) \otimes \boldsymbol{\eta}_D(v_r) \otimes \boldsymbol{\eta}_{\text{A}}(r) \ , \quad (11)$$

$$\eta_{\text{R},n}(r) = e^{-j2\pi a \frac{2r}{c} t_n} \ , \quad (12)$$

$$\eta_{\text{D},k}(v_r) = e^{-j\omega_c \frac{2v_r}{c} T_k} \ , \quad (13)$$

$$\eta_{\text{A},l}(\theta) = e^{j\frac{2\pi}{\lambda}\sin\theta d_l} \ , \quad (14)$$

The nuisance vector, $\mathbf{b}_q(r, v_r, v_\theta, \theta)$, satisfies

$$b_{q,l,k,n}(r, v_r, v_\theta, \theta) = e^{-j2\pi a \frac{2v_r}{c} t_n T_k} e^{-j2\pi a \frac{\bar{D}_q \sin\theta}{c} t_n} \times e^{j\frac{2\pi}{r\lambda} \bar{D}_q \cos^2\theta d_l} e^{j\frac{2\pi v_\theta \cos\theta}{r\lambda} d_l T_k} \ , \quad (15)$$

where the term $b_{q,l,k,n}(r, v_r, v_\theta, \theta)$ represents the $NKl + Nk + n^{\text{th}}$ element of the vector $\mathbf{b}_q(r, v_r, v_\theta, \theta)$. Lastly, the tangential velocity information vector, $\mathbf{z}_q(r, v_\theta, \theta)$. satisfies

$$\mathbf{z}_q(r, v_\theta, \theta) = \mathbf{1}_L \otimes \tilde{\mathbf{z}}_q(r, v_\theta, \theta) \otimes \mathbf{1}_N,$$

$$\tilde{z}_{q,k}(r, v_r, \theta) = e^{-j\omega_c \frac{v_\theta^2}{rc} T_k^2} e^{-j\frac{2\pi \bar{D}_q v_\theta \cos\theta}{r\lambda} T_k} \ . \quad (16)$$

The wide aperture separated array model in (10) consists of the conventional target range, radial velocity, and DOA estimation data vector, $\boldsymbol{\eta}(r, v_r, \theta)$. The term, $\mathbf{b}_q(r, v_r, v_\theta, \theta)$ is the nuisance elements vector, which contains the elements $e^{-j2\pi a \frac{2v_r}{c} T_k t_n}$ and $e^{j2\pi a \frac{\sin\theta}{c} d_l t_n}$, which include the fast-time variable t_n. Conventionally, elements that include fast-time variables appear in the term, $\boldsymbol{\eta}_{\mathrm{R}}(r)$, in (12). Therefore, one can infer that these elements are related to the range migration phenomenon, where $e^{-j2\pi a \frac{2v_r}{c} T_k t_n}$ is related to range migration along the observation time, and $e^{j2\pi a \frac{\sin\theta}{c} d_l t_n}$ is related to range migration along the array aperture.

III. Target Parameter Estimation

This section proposes the target parameter estimation approach using the model in Section II and focuses on tangential velocity estimation. The proposed iterative algorithm is based on the ML estimator for the model in (10).

Let $\mathbf{x} = \left[\mathbf{x}_0^T, \mathbf{x}_1^T\right]^T$ denote the concatenated vector of received radar echo. Using (10), the vector, $\mathbf{x}$, can be modeled as

$$\mathbf{x} = \left[\alpha_0 \mathbf{a}_0^T(\boldsymbol{\psi}), \alpha_1 \mathbf{a}_1^T(\boldsymbol{\psi})\right]^T + \left[\mathbf{w}_0^T, \mathbf{w}_1^T\right]^T = \mathbf{A}(\boldsymbol{\psi})\boldsymbol{\alpha} + \mathbf{w}\ , \tag{17}$$

where

$$\mathbf{A}(\boldsymbol{\psi}) = \begin{bmatrix} \mathbf{a}_0(\boldsymbol{\psi}) & \mathbf{0} \\ \mathbf{0} & \mathbf{a}_1(\boldsymbol{\psi}) \end{bmatrix}, \tag{18}$$

$$\boldsymbol{\alpha} = \left[\alpha_0, \alpha_1\right]^T, \tag{19}$$

$$\mathbf{a}_q(\boldsymbol{\psi}) = \boldsymbol{\eta}(r, v_r, \theta) \odot \mathbf{b}_q(r, v_r, \theta) \odot \mathbf{z}_q(r, v_\theta, \theta)\ , \tag{20}$$

and $\boldsymbol{\psi} = \left[r, v_r, v_\theta, \theta\right]^T$ is the vector of unknown parameters of interest. In this case, $\mathbf{x} \sim CN\left(\mathbf{A}(\boldsymbol{\psi})\boldsymbol{\alpha}, \sigma_w^2 \mathbf{I}_{2LNK}\right)$, and thus, the log-likelihood function for estimating $\boldsymbol{\xi} = \left[\alpha_{0,r}, \alpha_{0,i}, \alpha_{1,r}, \alpha_{1,i}, \boldsymbol{\psi}^T\right]^T$ from $\mathbf{x}$ is

$$LL(\boldsymbol{\xi}) = -2LNK \log 2\pi\sigma_w^2 - \frac{\left\|\mathbf{x} - \mathbf{A}(\boldsymbol{\psi})\boldsymbol{\alpha}\right\|^2}{\sigma_w^2}\ . \tag{21}$$

Optimization of (21) w.r.t. $\boldsymbol{\alpha}$, and ignoring constants will result in [40]

$$LL'(\boldsymbol{\psi}) = \mathbf{x}^H \mathbf{P}_{\mathbf{A}} \mathbf{x}\ , \tag{22}$$

where $\mathbf{P}_{\mathbf{A}} = \mathbf{A}(\boldsymbol{\psi})\left(\mathbf{A}^H(\boldsymbol{\psi})\mathbf{A}(\boldsymbol{\psi})\right)^{-1}\mathbf{A}^H(\boldsymbol{\psi})$ is the orthogonal projection matrix on the column space of $\mathbf{A}(\boldsymbol{\psi})$. According to (18) and (20), $\mathbf{A}^H(\boldsymbol{\psi})\mathbf{A}(\boldsymbol{\psi}) = 2NKL\mathbf{I}_2$, and $\mathbf{x}^H\mathbf{A}(\boldsymbol{\psi}) = \left[\mathbf{x}_0^H\mathbf{a}_0(\boldsymbol{\psi}), \mathbf{x}_1^H\mathbf{a}_1(\boldsymbol{\psi})\right]^T$. Therefore, for the non-coherent wide aperture separated array model in (10), the ML estimation is defined as

$$\hat{\boldsymbol{\psi}} = \arg\max_{\boldsymbol{\psi}} \left(\left|\mathbf{x}_0^H\mathbf{a}_0(\boldsymbol{\psi})\right|^2 + \left|\mathbf{x}_1^H\mathbf{a}_1(\boldsymbol{\psi})\right|^2\right)\ . \tag{23}$$

However, the straightforward implementation of (23) requires a 4D search, which can be computationally infeasible. Therefore, a computationally efficient algorithm that approximates (23) via coordinate descent is proposed in this work [41], and summarized in Algorithm 1. Throughout Algorithm 1, calligraphic letters represent reshaped vectors with the same data, for example $\mathcal{M} = \mathrm{reshape}(\mathbf{m}, N, K, L)$.

Lines 1-4 in Algorithm 1 present a triangulation estimation of v_θ, similar to [26]. The estimated parameters are used to compensate the data in line 5. In lines 5-8 the coordinated ascent approach begins with the estimation of r, v_r, θ, by applying the conventional 3D fast Fourier transform (FFT) on the compensated data. The total log-likelihood function (LF) for r, v_r, θ is constructed by the sum of the squares of both 3D-FFT maps, thus approximating (23).

Next, the second step of the coordinate ascent approach is executed by the estimation of v_r and v_θ. The velocities v_r and v_θ are simultaneously estimated, as they are strongly coupled on the slow time axis. The slow time correlator for the radial and tangential velocity estimation is defined as

$$\bar{\mathbf{z}}_q(r, v_r, v_\theta, \theta) = \tilde{\mathbf{z}}_q(r, v_\theta, \theta) \odot \boldsymbol{\eta}_{\mathrm{D}}(v_r)\ . \tag{24}$$

The slow-time correlator, $\bar{\mathbf{z}}_q(r, v_r, v_\theta, \theta)$, combines the v_θ near-field information in (16), and the conventional radial velocity estimation information in (13). First, lines 9-10 present an extraction of the slow-time data using the previous estimation of r, v_r, v_θ, θ, where $\times_n$ and $\times_l$ represent the tensor products on the fast-time and spatial axes, respectively. Lines 11-13 present the estimation of v_r and v_θ according to (23) and (24).

Algorithm 1 Single Target Parameters Estimation

Require: $\{\mathbf{x}_0, \mathbf{x}_1\}$ - Radar measurements from two subarrays.
Require: a, T_c, K, λ, T_{PRI}, L, N, $\bar{D}$, - chirp slope, chirp time, number of chirps, wavelength, PRI, number of sensors, number of samples per chirp, distance between the centers of the subarrays.
Require: ε - iterations termination criterion.

1: $\mathcal{LF}_{1,q}(r, v_r, \theta) = 3\mathrm{D} - \mathrm{FFT}(\mathcal{X}_q)$
2: $\left\{\hat{r}_q, \hat{v}_{r,q}, \hat{\theta}_q\right\} = \arg\max_{r, v_r, \theta} \left|\mathcal{LF}_{1,q}(r, v_r, \theta)\right|$
3: $\hat{r} = \frac{\hat{r}_0 + \hat{r}_1}{2}$, $\hat{v}_r = \frac{\hat{v}_{r,0} + \hat{v}_{r,1}}{2}$, $\hat{\theta} = \arcsin\left(\frac{\sin\hat{\theta}_0 + \sin\hat{\theta}_1}{2}\right)$
4: $\tilde{v}_\theta = \frac{2\hat{r}(\hat{v}_{r,0} - \hat{v}_{r,1})}{\bar{D}\cos\hat{\theta}}$
5: $\tilde{\mathbf{x}}_q = \mathbf{x}_q \odot \mathbf{b}_q^*\left(\hat{r}, \hat{v}_r, \tilde{v}_\theta, \hat{\theta}\right) \odot \mathbf{z}_q^*\left(\hat{r}, \tilde{v}_\theta, \hat{\theta}\right)$
6: $\mathcal{L}_q(r, v_r, \theta) = 3\mathrm{D} - \mathrm{FFT}\left(\tilde{\mathcal{X}}_q\right)$
7: $\mathcal{LF}_2(r, v_r, \theta) = \left|\mathcal{L}_0(r, v_r, \theta)\right|^2 + \left|\mathcal{L}_1(r, v_r, \theta)\right|^2$
8: $\left\{\hat{r}, \hat{v}_r, \hat{\theta}\right\} = \arg\max_{r, v_r, \theta} \mathcal{LF}_2(r, v_r, \theta)$
9: $\tilde{\mathbf{x}}_q = \mathbf{x}_q \odot \mathbf{b}_q^*\left(\hat{r}, \hat{v}_r, \tilde{v}_\theta, \hat{\theta}\right)$
10: $\mathbf{y}_q = \frac{1}{NL}\boldsymbol{\eta}_R^*(\hat{r}) \times_n \tilde{\mathcal{X}}_q \times_l \boldsymbol{\eta}_A^*\left(\hat{\theta}\right)$
11: $\mathbf{L}_q(v_r, v_\theta) = \left|\mathbf{y}_q^H \bar{\mathbf{z}}_q\left(\hat{r}, v_r, v_\theta, \hat{\theta}\right)\right|^2$
12: $\mathbf{LF}_3(v_r, v_\theta) = \mathbf{L}_0(v_r, v_\theta) + \mathbf{L}_1(v_r, v_\theta)$
13: $\{\hat{v}_r, \hat{v}_\theta\} = \arg\max_{v_r, v_\theta} \mathbf{LF}_2(v_r, v_\theta)$
14: **if** $|\tilde{v}_\theta - \hat{v}_\theta| \geq \varepsilon$ **then**
15: $\quad \tilde{v}_\theta = \hat{v}_\theta$
16: $\quad$ Return to 6.
17: **end if**
18: **return** $\left\{\hat{r}, \hat{v}_r, \hat{v}_\theta, \hat{\theta}\right\}$

In the multi-target scenario, the algorithm can be adapted to estimate the parameters of all targets, thus also addressing clutter-dominated scenarios.

IV. Performance Evaluation

The performance of the proposed algorithms for tangential velocity estimation is evaluated in this section. Consider a single target with the following parameters: $r = 90$ m, $v_r = -20$ m/sec, $v_\theta = 10$ m/sec, $\theta = 40°$. In addition, for simplicity we consider $|\alpha_0| = |\alpha_1|$. Fig. 2 shows the evaluated root mean-squared-error (RMSE) of Algorithm 1 as a function of SNR, defined as

$$\mathrm{SNR} = \frac{NKL\left(|\alpha_0|^2 + |\alpha_1|^2\right)}{\sigma_w^2} . \tag{25}$$

The RMSE performance is compared to the CRB for the model in (10), given by

$$C_{v_\theta, v_\theta}(\boldsymbol{\xi}) = \frac{r^2\lambda^2}{\pi^2 K^2 T_{\mathrm{PRI}}^2 (P_1 + P_2 + P_3)\,\mathrm{SNR}} , \tag{26}$$

$$P_1 = \frac{8\mathrm{NFSA}^2}{45} , \tag{27}$$

$$P_2 = \frac{D^2\cos^2\theta}{18} , \tag{28}$$

$$P_3 = \frac{\bar{D}^2\cos^2\theta}{6} , \tag{29}$$

where the physical aperture of each subarray is $D = L\lambda/2$, and the near-field synthetic aperture (NFSA) is defined as $\mathrm{NFSA} = |v_\theta K T_{\mathrm{PRI}}|$. The RMSE is evaluated over 1000 Monte-Carlo simulations for each SNR. The evaluated RMSE of Algorithm 1 achieves the CRB at $\mathrm{SNR} = 23$ dB. It can be observed that for $\mathrm{SNR} > 22$ dB, Algorithm 1 achieves the same performance as the straightforward ML estimator, which involves a 4D search procedure. Similarly, it can be shown that the algorithm achieves the CRB for the parameters, r, v_r, θ.

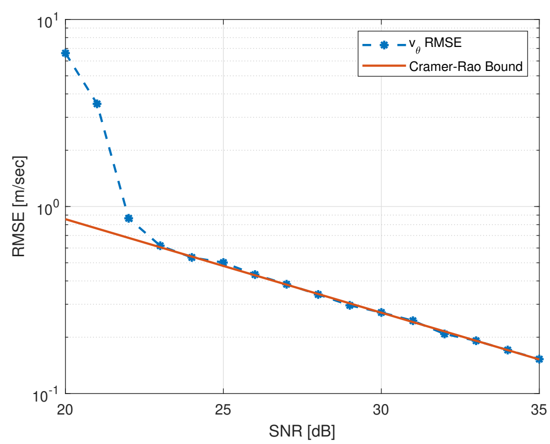

Fig. 2: RMSE of Algorithm 1 for estimating v_θ compared to the CRB versus SNR with target parameters $r = 90$ m, $v_r = -20$ m/sec, $v_\theta = 10$ m/sec, $\theta = 40°$, and radar parameters $\bar{D} = 50$ cm, $K = 2500$, $L = 50$, $T_{\mathrm{PRI}} = 20\ \mu$sec, $B = 250$ MHz, $f_c = 77$ GHz.

Fig. 3 shows the evaluated RMSE over 2000 Monte-Carlo simulations for each NFSA, $\bar{D} = \{10, 50, 100, 150\}$ cm, and $\mathrm{SNR} = 25$ dB. The NFSA grid is defined by setting the total observation time, KT_{PRI}, to 50 msec, and varying v_θ from 0 to 30 m/sec. Notice that for $\bar{D} = D = 10$ cm, the radar array configuration is ULA, resulting in v_θ sign ambiguity due to the small physical aperture of the ULA. A Slight increase in $\bar{D}$ allows to resolve the ambiguity in the sign of v_θ, as the RMSE for $\bar{D} = \{50, 100, 150\}$ cm is below 1m/sec for NFSA $<$ 100cm. Notice that for NFSA $<$ 100 cm and

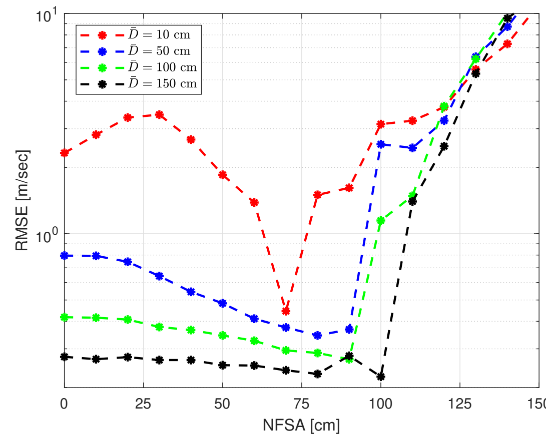

Fig. 3: The RMSE of Algorithm 1 for estimating v_θ versus NFSA for different subarrays separation, $\bar{D}$, with target parameters $r = 90$ m, $v_r = -20$ m/sec, $\theta = 40°$, $\mathrm{SNR} = 25$ dB and radar parameters $K = 2500$, $L = 50$, $T_{\mathrm{PRI}} = 20\ \mu$sec, $B = 250$ MHz, $f_c = 77$ GHz.

$\bar{D} = \{50, 100, 150\}$ cm, the RMSE decreases with increasing NFSA. However, the dependency of the RMSE on the NFSA decreases with increasing $\bar{D}$. This result stems from (26), as the proposed estimator achieves the CRB. According to (26), the CRB decreases with increasing the NFSA, and for sufficiently large $\bar{D}$, much larger NFSA is required for dependency of the CRB on the NFSA.

Notice that the RMSE increases with increasing NFSA for NFSA $\geq$ 100cm. This is due to the element $e^{-j\omega_c \frac{v_\theta^2 T_k^2}{rc}}$ in $\bar{\mathbf{z}}_q(r, v_\theta, \theta)$. In lines 1-2 of Algorithm 1, when r, v_r, and θ are estimated for each subarray, v_θ is assumed to be 0, and thereby ignoring the term $e^{-j\omega_c \frac{v_\theta^2 T_k^2}{rc}}$. Disregarding this term results in target "Doppler" migration along the observation time, due to the term T_k^2 in the phase. This migration phenomenon results in a loss of the magnitude in the r.h.s. of line 2 in Algorithm 1, which leads to higher threshold SNR. In the case of Fig. 3, $\mathrm{SNR} = 25$ dB is below the threshold Signal-to-Noise Ratio (SNR), which leads to an increased RMSE for NFSA $\geq$ 100 cm. To improve the peak magnitude, one is required to do estimate v_θ^2, and thus, one is required to do a 4D search.

V. Conclusion

This work introduces a wide aperture separated array automotive radar for tangential velocity estimation. An iterative algorithm for estimating the unknown target parameters, based on the ML is derived, and its performance for tangential velocity estimation was studied. The algorithm is shown to be asymptotically efficient, and its performance improves with increasing NFSA, up to a certain NFSA value where the Doppler migration along the slow-time becomes dominant.

References

[1] C. Waldschmidt, J. Hasch, and W. Menzel, “Automotive radar — from first efforts to future systems,” *IEEE J. of Microw.*, vol. 1, no. 1, pp. 135–148, 2021.

[2] A. Venon, Y. Dupuis, P. Vasseur, and P. Merriaux, "Millimeter wave FMCW radars for perception, recognition and localization in automotive applications: A survey," *IEEE Trans. on Intell. Vehicles*, vol. 7, no. 3, pp. 533–555, 2022.

[3] M. Murad, I. Bilik, M. Friesen, J. Nickolaou, J. Salinger, K. Geary, and J. S. Colburn, "Requirements for next generation automotive radars," in *2013 IEEE Radar Conf. (RadarCon13)*, 2013, pp. 1–6.

[4] I. Bilik, "Comparative analysis of radar and lidar technologies for automotive applications," *IEEE Intell. Transp. Syst. Mag.*, vol. 15, no. 1, pp. 244–269, 2023.

[5] I. Bilik, O. Longman, S. Villeval, and J. Tabrikian, "The rise of radar for autonomous vehicles: Signal processing solutions and future research directions," *IEEE Signal Process. Mag.*, vol. 36, no. 5, pp. 20–31, 2019.

[6] S. M. Patole, M. Torlak, D. Wang, and M. Ali, "Automotive radars: A review of signal processing techniques," *IEEE Signal Process. Mag.*, vol. 34, no. 2, pp. 22–35, 2017.

[7] G. Hakobyan and B. Yang, "High-performance automotive radar: A review of signal processing algorithms and modulation schemes," *IEEE Signal Process. Mag.*, vol. 36, no. 5, pp. 32–44, 2019.

[8] I. Bilik, S. Villeval, D. Brodeski, H. Ringel, O. Longman, P. Goswami, C. Y. B. Kumar, S. Rao, P. Swami, A. Jain, A. Kumar, S. Ram, K. Chitnis, Y. Dutt, A. Dubey, and S. Liu, "Automotive multi-mode cascaded radar data processing embedded system," in *2018 IEEE Radar Conf. (RadarConf18)*, 2018, pp. 372–376.

[9] M. I. Skolnik, *Introduction to Radar Systems*. McGraw-Hill Education, 2002.

[10] J. Hasch, E. Topak, R. Schnabel, T. Zwick, R. Weigel, and C. Waldschmidt, "Millimeter-wave technology for automotive radar sensors in the 77 GHz frequency band," *IEEE Trans. on Microw. Theory and Techn.*, vol. 60, no. 3, pp. 845–860, 2012.

[11] J. Tabrikian, O. Isaacs, and I. Bilik, "Cognitive antenna selection for DOA estimation in automotive radar," in *IEEE Radar Conf.*, 2016, pp. 1–5.

[12] E. Arnold, O. Y. Al-Jarrah, M. Dianati, S. Fallah, D. Oxtoby, and A. Mouzakitis, "A survey on 3D object detection methods for autonomous driving applications," *IEEE Trans. on Intell. Transp. Syst.*, vol. 20, no. 10, pp. 3782–3795, 2019.

[13] F. Folster and H. Rohling, "Lateral velocity estimation based on automotive radar sensors," in *2006 CIE Int. Conf. on Radar*, 2006, pp. 1–4.

[14] J. Merlo, E. Klinefelter, and J. A. Nanzer, "Three-dimensional velocity measurement using a dual axis millimeter-wave interferometric radar," *IEEE Trans. on Microw. Theory and Techn.*, vol. 70, no. 3, pp. 1674–1685, 2022.

[15] Y. Zhang and S. Wang, "Remote relative wind velocity estimation using airborne Doppler radar and spectrum analysis," *IEEE Trans. on Aerosp. and Electron. Syst.*, vol. 47, no. 3, pp. 1648–1667, 2011.

[16] J. Moreira and W. Keydel, "A new MTI-SAR approach using the reflectivity displacement method," *IEEE Trans. on Geosci. and Remote Sens.*, vol. 33, no. 5, pp. 1238–1244, 1995.

[17] L. Mei, W. Pengfei, W. Zhigui, and L. Chenlei, "Multidimensional motion parameters' estimation for multi-SAR system using the cubic phase function," *IEEE Trans. on Geosc. and Remote Sens.*, vol. 56, no. 6, pp. 3210–3221, 2018.

[18] S. S. Ram, "Fusion of inverse synthetic aperture radar and camera images for automotive target tracking," *IEEE J. of Sel. Topics in Signal Process.*, vol. 17, no. 2, pp. 431–444, 2023.

[19] H. Rohling, F. Folster, and H. Ritter, "Lateral velocity estimation for automotive radar applications," in *2007 IET Int. Conf. on Radar Syst.*, 2007, pp. 1–4.

[20] P. R. M. de Araujo, A. Noureldin, and S. Givigi, "Toward land vehicle ego-velocity estimation using deep learning and automotive radars," *IEEE Trans. on Radar Syst.*, vol. 2, pp. 460–470, 2024.

[21] S. A. Askeland and T. Ekman, "Tracking with a high-resolution 2D spectral estimation based automotive radar," *IEEE Trans. on Intell. Transp. Syst.*, vol. 16, no. 5, pp. 2418–2423, 2015.

[22] M. Pilté, S. Bonnabel, and F. Barbaresco, "An innovative nonlinear filter for radar kinematic estimation of maneuvering targets in 2D," in *2017 18th Int. Radar Symp. (IRS)*, 2017, pp. 1–10.

[23] M. Gottinger, M. Hoffmann, M. Christmann, M. Schütz, F. Kirsch, P. Gulden, and M. Vossiek, "Coherent automotive radar networks: The next generation of radar-based imaging and mapping," *IEEE J. of Microw.*, vol. 1, no. 1, pp. 149–163, 2021.

[24] V. Janoudi, P. Schoeder, T. Grebner, N. Appenrodt, J. Dickmann, and C. Waldschmidt, "On distributed radar networks: Signal model, analysis, and signal processing," *IEEE J. of Microw.*, vol. 4, no. 3, pp. 329–347, 2024.

[25] S.-G. Lee, J. Jung, and S.-C. Kim, "Enhanced velocity vector estimation using distributed radar system," in *2022 IEEE VTS Asia Pacific Wireless Commun. Symp. (APWCS)*, 2022, pp. 75–79.

[26] J. A. Nanzer, "Millimeter-wave interferometric angular velocity detection," *IEEE Trans. on Microw. Theory and Techn.*, vol. 58, no. 12, pp. 4128–4136, 2010.

[27] T. Song, X. Yao, L. Wang, Y. Wang, and G. Sun, "Fast factorized Kirchhoff migration algorithm for near-field radar imaging with sparse MIMO arrays," *IEEE Trans. on Geosc. and Remote Sens.*, vol. 62, pp. 1–14, 2024.

[28] Y. Liu, M. Tao, T. Shi, J. Wang, J. Wang, and X. Mao, "Sub-aperture polar format algorithm for curved trajectory millimeter wave radar imaging," *IEEE Trans. on Radar Syst.*, vol. 2, pp. 67–83, 2024.

[29] J. W. Smith and M. Torlak, "Efficient 3-D near-field MIMO-SAR imaging for irregular scanning geometries," *IEEE Access*, vol. 10, pp. 10 283–10 294, 2022.

[30] A. Sommer, T. T. Ngo, and J. Ostermann, "3D multiple input single output near field automotive synthetic aperture radar," in *2017 18th Int. Radar Symp. (IRS)*, 2017, pp. 1–10.

[31] A. Sakhnini, S. De Bast, M. Guenach, A. Bourdoux, H. Sahli, and S. Pollin, "Near-field coherent radar sensing using a massive MIMO communication testbed," *IEEE Trans. on Wireless Commun.*, vol. 21, no. 8, pp. 6256–6270, 2022.

[32] H. Hua, J. Xu, and Y. C. Eldar, "Near-field 3D localization via MIMO radar: Cramér-Rao bound analysis and estimator design," *IEEE Trans. on Signal Process.*, vol. 72, pp. 3879–3895, 2024.

[33] H. Wang, Z. Xiao, and Y. Zeng, "Cramér-Rao bounds for near-field sensing with extremely large-scale MIMO," *IEEE Trans. on Signal Process.*, vol. 72, pp. 701–717, 2024.

[34] H. Chen, J. Fang, W. Wang, W. Liu, Y. Tian, Q. Wang, and G. Wang, "Near-field target localization for EMVS-MIMO radar with arbitrary configuration," *IEEE Trans. on Aerosp. and Electron. Syst.*, vol. 60, no. 4, pp. 5406–5417, 2024.

[35] L. Khamidullina, I. Podkurkov, and M. Haardt, "Conditional and unconditional Cramér-Rao bounds for near-field localization in bistatic MIMO radar systems," *IEEE Trans. on Signal Process.*, vol. 69, pp. 3220–3234, 2021.

[36] Q. Shen, W. Liu, L. Wang, and Y. Liu, "Group sparsity based localization for far-field and near-field sources based on distributed sensor array networks," *IEEE Trans. on Signal Process.*, vol. 68, pp. 6493–6508, 2020.

[37] M. N. E. Korso, R. Boyer, A. Renaux, and S. Marcos, "Conditional and unconditional Cramér–Rao bounds for near-field source localization," *IEEE Transactions on Signal Processing*, vol. 58, no. 5, pp. 2901–2907, 2010.

[38] M. Shifrin, J. Tabrikian, and I. Bilik, "Identifiability study of near-field automotive SAR," in *Int. Conf. of Acoust. and Signal Process.*, Seoul, South Korea, Apr. 14-19, 2024.

[39] I. Bilik, J. Tabrikian, and A. Cohen, "GMM-based target classification for ground surveillance Doppler radar," *IEEE Trans. on Aerosp. and Electron. Syst.*, vol. 42, no. 1, pp. 267–278, 2006.

[40] S. M. Kay, *Fundamentals of Statistical Signal Processing*, ser. Prentice-Hall signal processing series. Englewood Cliffs, N.J: Prentice-Hall PTR, 1993 - 1998.

[41] S. J. Wright, "Coordinate descent algorithms," *Math. Program.*, vol. 151, no. 1, pp. 3–34, 2015.